Section 3

Computational studies including new techniques, the effect of varying model resolution, parallel processing

The benefits of increased resolution in simulating precipitation over Sub-Saharan Africa.
## A comparison of AMIP integrations of GEM at 1° and 2° model resolution.

Anne Sophie Daloz, Colin Jones
Université du Québec à Montréal
daloz@sca.uqam.ca

Introduction

The Sub-Saharan tropical climate is mainly driven by the seasonal migration of the ITCZ (Inter Tropical Convergence Zone). Within the ITCZ strong scale interaction supports the development of African Easterly Waves (AEWs), with Mesoscale Convective Systems (MCS) embedded within these synoptic scale waves. The latter MCS are responsible for much of the precipitation in the sub-Saharan region (Lebel et al., 2003). Substantial differences have been documented in the meridional migration and intensity of the ITCZ between wet and dry years (Grist and Nicholson 2001), with large impacts on local populations. The aim of this study is to investigate the ability of 2 versions of the Global Environmental Model (GEM) to simulate precipitation variability over Sub-Saharan Africa, both in terms of the climatological annual cycle and interannual variability.

Model and Observations

Simulated data is obtained from an AMIP-style integration of the Global version of GEM, forced by observed Sea Surface Temperatures (SST) for the period 1978-2003. Two versions of GEM are compared, at resolutions of 1° and 2° respectively. GEM uses the Kain-Fristch convection scheme (Kain and Fritsch 1990) which amongst other features includes a resolution dependent convective trigger function. In this study we wish to compare the impact of increased resolution on simulated precipitation over sub-Saharan Africa. Model results are compared to observations from the Global Precipitation Climatology Project (GPCP) pentad precipitation data set at 2.5° resolution for the period 1979-2003. All results have been interpolated to a common 2.5° grid.
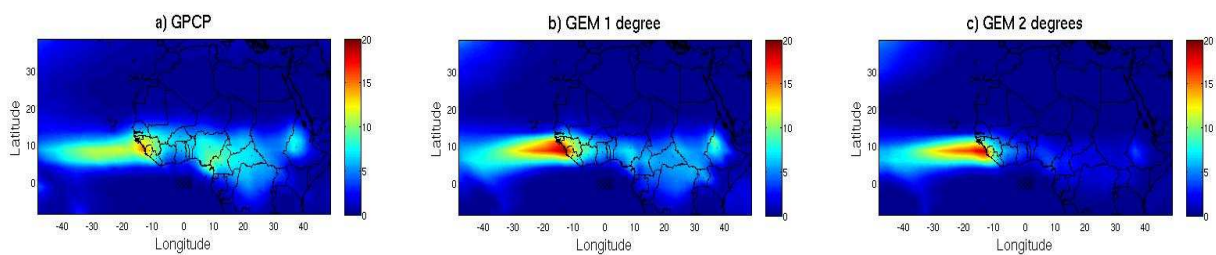

Figures 1 *Climatological seasonal mean (JAS, July, August, and September) precipitation (mm/day) for: a) GPCP. b) GEM 1° and c) GEM2°. for 1979-2003.*

Results

Figure 1 shows the 1979-2003 averaged seasonal mean precipitation for the months June-August (JJA). The GEM 2° integration significantly underestimates precipitation across the African ITCZ region, while the GEM 1° results are clearly improved, although still underestimated by ~20% compared to GPCP values. Local maxima in precipitation are well captured around the Ethiopian highlands (35-40°W, 10°N) and at the Atlantic coast. The latter maxima appears somewhat overestimated in both GEM integrations, although TRMM climatology (1998-2003) suggests more like 16-18 mm/day in this region and GPCP values around 14-16 mm/day.

To better evaluate the seasonal migration of the ITCZ, figure 2 presents a latitude versus time analysis of precipitation, averaged over the longitude belt 20°W-40°E (i.e. the continental Africa ITCZ) and for the years 1979-2003. Differences between the 2 GEM integrations and the GPCP values are shown in figure 2c and 2d. Both the ITCZ intensity and northward propagation are significantly improved in the 1° version of GEM. The onset and decay of the rainy season are also relatively well captured, with the main error being excess precipitation in the early part of the wet season (May-June).
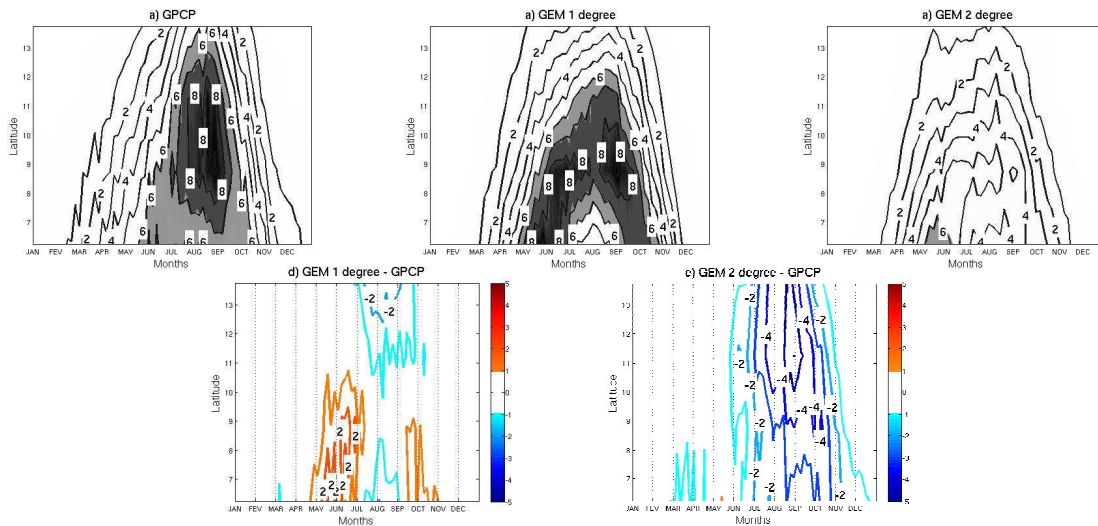
Figures 2 *Cross section of mean rainfall (mm.day⁻¹) as a function of month and latitude, averaged for 20°W to 40°E from 1979 to 2003 for: a) GPCP, b) GEM of 1 degree resolution, c) for GEM with a resolution of 2 degrees, d) GEM 1 degree minus GPCP observations and e) GEM 2 degrees minus GPCP observations.*

Conclusions

This work clearly shows the benefits of increased resolution in the GEM global atmospheric model in terms of simulating the climatology of precipitation over sub-Saharan Africa. Both the location, intensity and seasonal migration are significantly improved when the resolution of GEM, is increased from 2° to 1°. Further work will look at the benefits ensuing with respect to simulated inter-annual variability of precipitation in this region and higher time frequency precipitation intensities.

References

Avila, L.A., and R.J. Pasch, 1992: Atlantic tropical systems of 1991. *Mon.Wea.Rew,* **120**, 2688-2696.

Burpee, R.W., 1972: The origin and structure of easterly waves in the lower troposphere. *J.Atmos. Sci.*, **29**,77-90.

Grist, P. G. and S. E. Nicholson, 2001: A study of the dynamics factors influencing the rainfall variability in the West African Sahel. *Journal of Climate*, **14**, 1337-1359.

Lebel, C.A., Diedhiou, A. and Laurent, H., 2003: Seasonal cycle and interannual variability of the Sahelian rainfall at the hydrological scales. *J. Geo. Res.*, **108**, 8389, doi10.1029/2001JD001580.

Mekonnen, A., C. D. Thorncroft and A. R. Aiyyer, 2006: Analysis of convection and its association with African Easterly waves. *Journal of Climate*, **19**, 5405-5421.

Development of the nonhydrostatic dynamical core for SL–AV model

Fadeev R. Yu., Tolstykh M. A.

Institute of Numerical Mathematics, Russian Academy of Sciences,
and Hydrometcentre of Russia, Moscow RUSSIA
email: lord.rrd@gmail.com, tolstykh@inm.ras.ru

The two-dimensional (in vertical plane) nonhydrostatic dynamical core was developed in the framework of the global finite-difference semi-Lagrangian model SL-AV [1].

The basic nonhydrostatic equations of the atmosphere as well as the general idea of their solution are similar to those of the semielastic semi-implicit semi-Lagrangian NH HIRLAM model [2], except that the momentum equation is replaced by the horizontal divergence equation. This approach provides an efficient numerical algorithm for solving the nonhydrostatic equations of the atmosphere.

The dynamical core employs vorticity-divergence formulation on the unstaggered grid (vorticity equation is absent for 2D vertical plane case). Furthermore, the SETTLS integration scheme [3] is applied instead of the classical two-time level semi-Lagrangian scheme used in NH HIRLAM. We also changed the geopotential calculation procedure from the midpoint rule to the trapezoidal rule. Another difference from the NH HIRLAM model is that we calculate the horizontal derivatives using the fourth–order scheme instead of the second–order algorithm.

A number of tests modeling the atmospheric processes with strong nonhydrostatic effects is carried out. The first test consists of a high–resolution adiabatic simulation with the artificial orography. The conditions of this experiment were as close as possible to those given in [4]. The time step was 6 s. For the vertical coordinate we used 101 layers (with constant $\Delta\sigma$) and the horizontal grid interval was 400 m covering a domain of about 160 km. The deviation of the horizontal wind from the basic state after 9000 s is shown in Fig. 1, left with the contour interval of 0.5 m/s. The area shown extends 20 km on each side of the center of the mountain and from 0 to 8 km in the vertical.

There are some differences in comparison with both analytical solution by Xue [4] (Fig. 1, right) and numerical solution by Janjic [5]. The reason of these differences is being investigated.

The numerical solution of the warm–bubble test [6] presented on Fig. 2 is in a good agreement with [5]. The time step in this experiment was 2 s (which can be compared to 0.3 s time step in [5]). The grid was represented by 101 vertical layers (100 m grid resolution from the Earth surface to 8 km) and by 400 horizontal nodes (100 m resolution). The maxima of the initial disturbance of the potential temperature from its neutral value of 300 K is 6.6 K. Initial position of disturbance is (0; 2750 m) with the diameter of 2500 m.
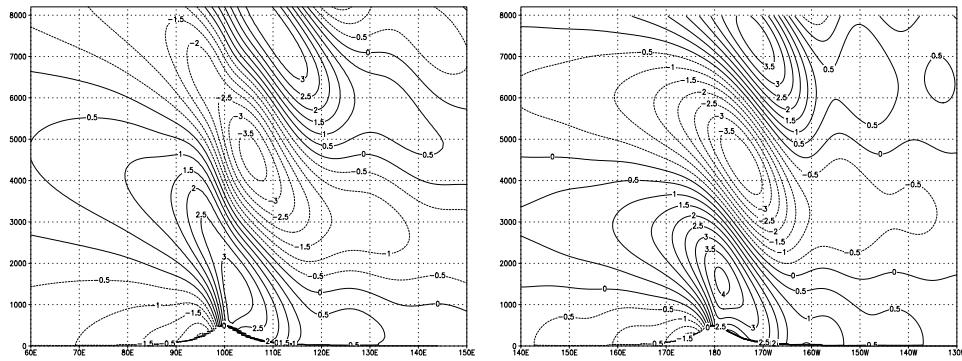
Figure 1: The deviation of the horizontal wind from its basic–state uniform value (10 m/s) after 9000 s. Left – numerical solution, right – analytical solution. The height of the bell shaped hill was 500 m, and its half–width was 2000 m. The Brunt–Vaisala stability parameter N is approximately 0.01 1/s.
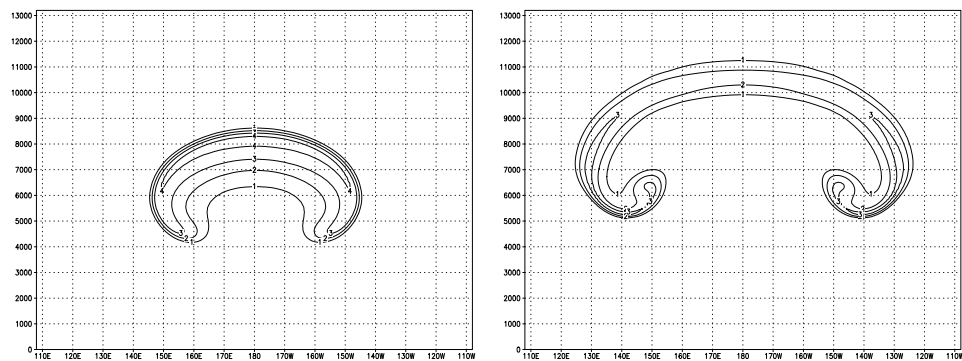

Figure 2: The potential temperature deviation after 900 s (left) and 1260 s (right) in the warm bubble test. The contour interval is 1 K.

References

[1] Tolstykh M. A. Semi–Lagrangian high resolution model of atmosphere for numerical weather prediction. – Russ. Meteor. and Hydrol., 2001, N 4, pp. 1–9.

[2] Rööm R., Männik A., Luhamaa A. Non-hydrostatic semi-elastic hybrid-coordinate SISL extension of HIRLAM. Part I: Numerical scheme. – Tellus, 2007, V. 59A, p. 650–660

[3] Hortal M. The development and testing of a new two–time–level semi–Lagrangian scheme (SETTLS) in the ECMWF forecast model. – Quart. J. Roy. Met. Soc., 2002, vol. 128, pp. 1671–1687.

[4] Xue M., et. al. Advanced regional prediction system. ARPS version 4.0 User's guide, center for analysis and prediction of storms, National Science Foundation, Federal Aviation Administration, The University of Oklahoma, 380 pp.

[5] Janjic Z. I., Gerrity Jr. J. P. An alternative approach to nonhydrostatic modeling. – Mon. Wea. Rev., 2000, vol. 129, pp. 1164–1178.

[6] Drogemeier K. The numerical simulation of thunderstorm outflow dynamics. Ph.D. dissertation, University of Illinois at Urbana–Champaign, 695 pp.

SGMIP-2 (Stretched-Grid Model Intercomparison Project): Decadal Regional Climate Simulations with Enhanced Variable and Uniform-Resolution GCMs

Michael Fox-Rabinovitz, University of Maryland at CollegePark, U.S.A., Jean Côté and Bernard Dugas, Environment Canada, Canada, Michel Déqué, Météo-France, France, John L. McGregor, CSIRO, Australia, and Alexei Belochitski, University of Maryland at College Park, U.S.A

Variable-resolution GCMs using a global stretched-grid (SG) with enhanced resolution over the region(s) of interest constitute an established approach to regional climate modeling providing an efficient means for regional down-scaling to mesoscales. This approach has been used since the early-mid 90s by the French, U.S., Canadian, Australian and other climate modeling groups along with, or as an alternative to, the current widely-used nested-grid approach. Stretched-grid GCMs are used for continuous climate simulations as usual GCMs, with the only difference that variable-resolution grids (Fig. 1) are used instead of more traditional uniform grids. The advantages of variable-resolution stretched-grid GCMs are that they do not require any lateral boundary conditions/forcing and are free of the associated undesirable computational problems. As a result, stretched-grid GCMs provide self-consistent interactions between global and regional scales while a high quality of global circulation is preserved, as in uniform-grid GCMs.

The international SGMIP-2 (Stretched-Grid Model Intercomparison Project, phase-2) includes 25-year (1979-2003) climate simulations using enhanced variable and uniform-resolution (UG)- GCMs developed at major centers/groups in Australia, Canada, France, and the U.S. The SGMIP-2 high resolution regional (North American) and global multi-model ensemble products are analyzed in recent papers (Fox-Rabinovitz et al. 2006, 2008) and are available as a link to the WMO/WCRP/WGNE web site: http://collaboration.cmc.ec.gc.ca/science/wgne.

The major SGMIP-2 conclusions are as follows.

1. High quality of global simulated products is obtained for SG-GCMs and UG-GCMs.

2. Regional climate variability for the SGMIP-2 ensembles, analyzed using both time mean spatial and temporal prognostic and diagnostic products, represents well the climate variability shown in observations or reanalysis.

3. Over the region of interest: (a) SG-GCMs with $0.5° \times 0.5°$ regional resolution have overall smaller errors, than those of the intermediate ($1° \times 1°$) uniform-grid (UG)-GCMs with the same number of global grid point as for the SG-GCMs; and (b) SG-GCMs and fine ($0.5° \times 0.5°$) resolution UG-GCMs have overall similar errors.

4. The positive impact from enhanced regional resolution on efficient downscaling to realistic mesoscales is obtained. Small regional biases are a fraction (~50% or less) of observational or reanalysis errors), and overall, regional biases are within the uncertainties of available observations and/or reanalysis.

5. The SGMIP-2 results showed that using a multi-model ensemble for the state-of-the-art SG-GCMs is beneficial for reducing the uncertainty of the multi-decadal regional climate simulation with enhanced regional resolution.

6. Orographically induced precipitation and other SGMIP-2 prognostic and diagnostic fields (such as temperature, winds, moisture, sea-level pressure, and hydrological cycle components) are well simulated at meso- and larger scales due to high-resolution regional forcing. The major positive regional impact from stretching is obtained from better resolved model dynamics and regionally-enhanced resolution of stationary lower-boundary forcing (orography). In that sense, the

improvements are obtained near small-scale terrain features and are reflected, for example, in the Appalachian area precipitation.

7. Regional spectra for SG-GCM and fine (0.5° × 0.5°) UG-GCM ensembles are close to each other and closer to reanalysis than the spectrum for the intermediate (1° × 1°) UG-GCM (Fig. 2).

8. SGMIP-2 shows better results than those of SGMIP-1 due to its increased integration period.

9. The SGMIP-2 products provide the practical possibility of creating joint, with the NARCCAP (North American Regional Climate Change Assessment Program) and other groups, regional multi-model ensembles for nested- and stretched-grid models which may be beneficial for the national and international regional climate modeling communities.

The SGMIP products and analysis results are available to national and international programs and groups such as WMO/WGNE, NARCCAP, CLIVAR, and IPCC.

SGMIP-2 was endorsed by the WMO/WCRP/WGNE at its annual meetings in 2004 – 2007.
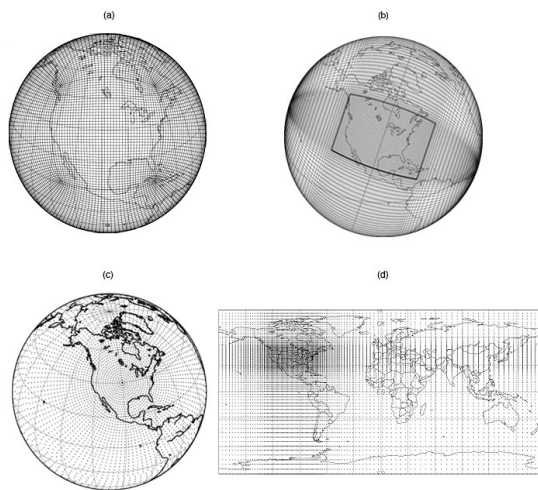

Fig. 1 SGMIP stretched grids with the area of interest over the major part of North America used in the following SG-GCMs: (a) CCAM, CSIRO, Australia; (b) GEM, Environment Canada; (c) ARPEGE, MeteoFrance; (d) GEOS, NASA/UMD,
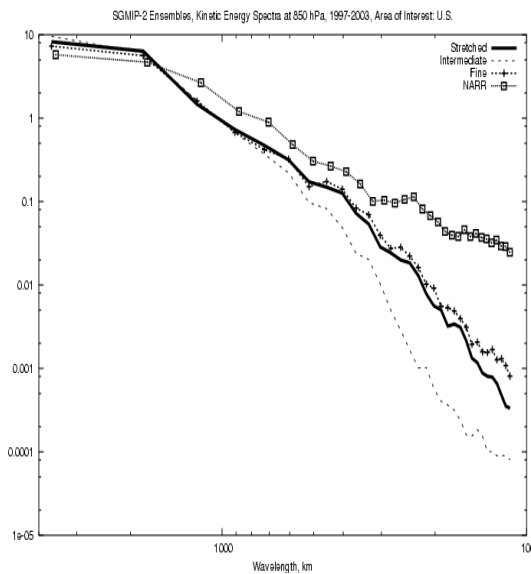U.S. Every other grid-line is shown.

Fig. 2 Regional energy spectra at the 850 hPa level for: the SG-GCM ensemble (the solid line), the intermediate uniform-resolution UG-GCM ensemble (the dotted line), the fine uniform-resolution UG-GCM ensemble (the solid-cross line), and the NARR reanalysis (the square-solid line). The logarithmic scales are used for both the x,y axes.

References

1. Fox-Rabinovitz, M.S., J. Côté, B. Dugas, M. Déqué, and J.L. McGregor, 2006a: Variable resolution general circulation models: Stretched-grid model intercomparison project (SGMIP), *J. Geophys. Res.,* 111, D16104, doi:10.1029/2005JD006520.

2. Fox-Rabinovitz, M.S., J. Côté, B. Dugas, M. Déqué, J.L. McGregor, and A. Belochitski, 2008: Stretched-Grid Model Intercomparison Project: Decadal regional climate simulations with enhanced variable and uniform-resolution GCMs, *Meteor. Atm. Phys.*, accepted.

Accurate and Fast Neural Network Emulations of Long Wave Radiation for the NCEP Climate Forecast System Model: Preliminary Results

V.M. Krasnopolsky[1,2,] E-mail: Vladimir.Krasnopolsky@noaa.gov,
M. S. Fox-Rabinovitz[2], S. J. Lord[1], Y.-T. Hou[1], and A. A. Belochitski[2]
[1]Environmental Modeling Center, NCEP/NOAA,
[2]Earth System Science Interdisciplinary Center, University of Maryland, USA

The approach to calculation of model physics using accurate and fast neural network (NN) emulations, has been previously proposed, developed and thoroughly tested by the authors for NCAR CAM [*Krasnopolsky et al. 2005,2008*]. In this study the NN approach has been introduced and tested in the NCEP climate forecast system (CFS) model. NN emulations of model physics approximate the functional dependence between inputs and outputs of a parameterization. They learn this functional dependence during the NN training utilizing a training data set which was simulated using the original parameterization.

The model radiation is the most time consuming component of model physics in CFS. This study is the first step in developing the NN emulations of the full CFS model radiation. Namely, the NN emulations have been developed and tested for the original long-wave radiation (LWR) parameterization for the CFS model [*Mlawer et al.* 1997].

Table 1. Statistics estimating the accuracy of heating rates (HRs) (in K/day) calculations and computational performance for NCEP LWR using NN emulation vs. the original parameterization. Bias$_0$ and RMSE$_0$ (in K/day) correspond to the lowest layer. NN60, NN75, and NN85 denote NN emulations with k = 60, 75, and 85 in eq. (1), respectively.

NN	Bias (K/day)	RMSE (K/day)	PRMSE (K/day)	Bias$_0$ (K/day)	RMSE$_0$ (K/day)
NN 60	$6. \cdot 10^{-3}$	0.44	0.35	$1. \cdot 10^{-3}$	0.68
NN 75	$1. \cdot 10^{-3}$	0.40	0.30	$-1. \cdot 10^{-2}$	0.57
NN 85	$3. \cdot 10^{-3}$	0.39	0.30	$2. \cdot 10^{-2}$	0.57

Table 1 shows bulk validation statistics for the accuracy of approximation and computational performance for the some developed NNs emulations. The accuracy of NN emulations is estimated against the original CFS LWR. For definitions of the error statistics (Bias, RMSE, PRMSE, etc.) see [*Krasnopolsky et al., 2005*]. PRMSE shown in the Table is the RMSE for the entire profile. For these NN emulations, bias is negligible and RMSE is limited. Obtaining very small NN emulation biases is important for providing non-accumulating errors in the course of model integrations using NN emulations. The developed highly accurate NN emulations for LWR, in terms of code-by-code comparison at each model time step when LWR is calculated, are about two orders of magnitude faster than the original/control NCEP CFS LWR.

The next step is validation of LWR NN emulation in the CFS model integrations. The LWR emulation NN75 was selected for such an initial validation in the CSF model runs because it seems to be acceptable in terms of both its accuracy and minimal complexity. The results of the 2-year (2005-2006) CFS model integration performed with NN75 emulation have been validated against the parallel control NCEP CFS model integration using the original LWR. The comparison of instantaneous model prognostic and diagnostic fields produced for the first week of model integrations shows that the differences are comparable with observational errors or uncertainties of data analysis. The comparison of time averaged (for the first four seasons and for two years) model prognostic and diagnostic fields shows a close similarity for the parallel runs. The 2-year mean

upward LWR flux at the top of the atmosphere presented in Fig. 1 shows similar distributions for the parallel runs (the left and center panels), with small differences or bias (the right panel). Bias for the extratropics is close to 0 and does not exceed by magnitude 5 W/m² within just a few spots. Bias in the tropics is also limited to the ±5 W/m² range and does not exceed by magnitude 10 – 15 W/m².

The further steps will include refinement of NN emulations for the CFS model, introduction of the concept of a compound parameterization including a quality control procedure [Krasnopolsky et al. 2008]**,** and the NN ensemble approach [Fox-Rabinovitz et al. 2006]. The developed methodology will be applied to short wave radiation to obtain NN emulations for the full/entire radiation block of the CFS model. The NN emulations will be also applied and validated for the GFS 10-day forecasts.
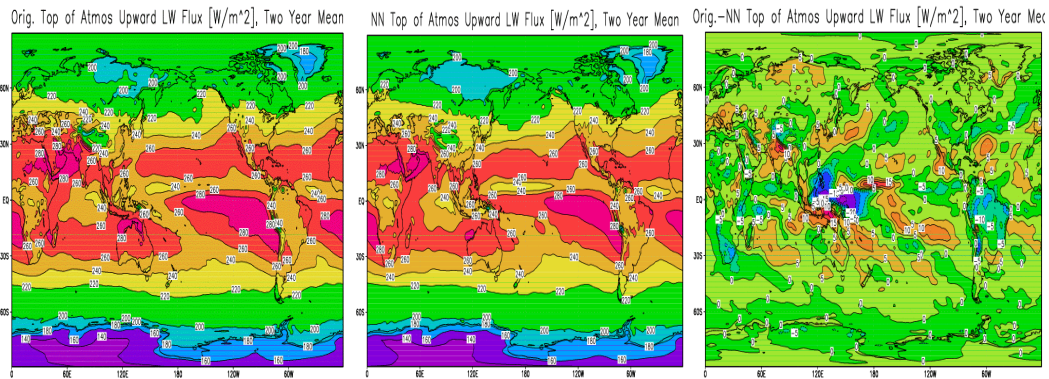

Fig. 1 2-year mean upward LWR flux at the top of the atmosphere, in W/m², for the CFS model integrations with: the original LWR (the left panel), the LWR NN75 emulation (the center panel), and their difference or bias (the right panel). The contour interval for the left and center panels is 20 W/m², and for the right panel is 5 W/m².

References

Fox-Rabinovitz M. S., V. Krasnopolsky, and A. Belochitski, 2006: "Ensemble of Neural Network Emulations for Climate Model Physics: The Impact on Climate Simulations", Proc., 2006 International Joint Conference on Neural Networks, Vancouver, BC, Canada, July 16-21, 2006, pp. 9321-9326, CD-ROM

Krasnopolsky, V.M., M.S. Fox-Rabinovitz, and D.V. Chalikov, 2005: "Fast and Accurate Neural Network Approximation of Long Wave Radiation in a Climate Model", *Monthly Weather Review*, vol. 133, No. 5, pp. 1370-1383.

Krasnopolsky, V. M., M.S. Fox-Rabinovitz, and A. A. Belochitski, 2008: "Decadal Climate Simulations Using Accurate and Fast Neural Network Emulation of Full, Long- and Short Wave, Radiation, *Monthly Weather Review,* in press.

Krasnopolsky, V.M., M.S. Fox-Rabinovitz, H.L. Tolman, and A. A. Belochitski, 2008: "Neural Network Approach for Robust and Fast Calculation of Physical Processes in Numerical Environmental Models: Compound Parameterization with a Quality Control of Larger Errors", *Neural Networks*, *doi:10.1016/j.neunet.2007.12.019* .

Mlawer, E.J., S.J. Taubman, P.D. Brown, M.J. Iacono, and S.A. Clough, 1997: "Radiative transfer for inhomogeneous atmospheres: RRTM, a validated correlated-k model for the longwave, *J. Geophys. Res.***,** 102, D14, 16,663-16,682

EXPERIMENTS WITH REGULARIZATION OF THE GEODESIC ICOSAHEDRAL GRID

Janusz A. Pudykiewicz, RPN, Environment Canada, e-mail: Janusz.Pudykiewicz@ec.gc.ca

The geodesic grid obtained from the iterative process of division of the icosahedron imbedded in a sphere offers certain advantages in the simulation of fluid flow on the sphere such as quasi-homogeneity and elimination of the pole problem typical for the standard latitude-longitude meshes. The ratio of the maximum to the minimum mesh interval ($\gamma = \delta_{\max}/\delta_{\min}$) for the icosahedral grid is slightly higher than one (1.2 for grid of level 4). This property is not unusual in the practice of computational fluid dynamics where variable grids are used quite commonly. Unfortunately, when analyzing the distribution of the grid interval on the surface of the sphere one can notice the pronounced discontinuities of the mesh interval as depicted in Fig. 1. Sudden changes of the grid properties can lead to generation of spurious vorticity, and consequently, to systematic errors when solving the partial differential equations on geodesic grid.

In order to alleviate this problem, the grid have to be regularized. One of the most popular options is the application of the, so called, spring dynamics (Tomita et al., 2001) in which the nodal points of the grid are connected by springs creating thus a large set of coupled harmonic oscillators. The time evolution of such system is governed by the following system of equations

$$\sum_{j(i)} k((\|\mathbf{r}_i - \mathbf{r}_j\| - \hat{d})\mathbf{e}_{ij} - \alpha \mathbf{w}_i = M_i \frac{d\mathbf{w}_i}{dt}, \quad \mathbf{w}_i = \frac{d\mathbf{r}_i}{dt} \tag{1}$$

where $\mathbf{r}_i$ is the position of the i-th node, $M_i = 10^4$, $k = 10^{-4}$, $\alpha = 10$, $\mathbf{e}_{ij} = \mathbf{r}_j - \mathbf{r}_i$, $\hat{d} = (2\beta\pi R)/(10 \times 2^{l-1})$ is the equilibrium spring length, $\beta = 0.4$ and l is the number of partitions of the icosahedron used to generate grid. The oscillating nodal points equilibrate after some time depending on the selected values of the parameters. The distribution of the nodal points obtained after the system achieves a state of the minimum energy is much more regular than that for the standard grid. The sample result for the grid of level four after 250 time steps with the 4-th order Runge-Kutta scheme ($\triangle t = 100$ s.) when the masses ceased to move is depicted in Fig. 2. The regularization of the grid, however, is associated with the increase of γ (for the case of grid level four γ increases from 1.2 to 1.5). This problem can be reduced by the use of nonlinear spring rates as suggested by Tomita et al. (2001). The alternative approach to the icosahedral grid regularization is based on the fundamental theorem of differential geometry. According to the Theorema Egregia of Gauss, the Laplace-Beltrami operator on manifold $\mathcal{M}$ can be expressed as follows

$$\triangle_{\mathcal{M}} p = -2H(p) \in \mathbf{R}^3 \tag{2}$$

where $H(p)$ is the mean curvature normal at $p \in \mathcal{M}$, and $\mathcal{M}$ is the two dimensional manifold in $\mathbf{R}^3$. After relation (2) is discretized on a standard icosahedral grid approximating $\mathcal{M} \equiv \{\mathbf{r} \in \mathbf{R}^3 : \|\mathbf{r}\| = a\}$, there is a relatively pronounced error caused by the sudden changes of the mesh interval depicted in Fig. 1. The error of approximation of (2) can be reduced by the proper redistribution of the nodal points using the following iteration

$$p_i^{n+1} = -\left(\frac{a^2}{2}\right) \mathbf{L} p_i^n \tag{3}$$

where $p_i^k \in \mathbf{R}^3$, a is the radius of the sphere, and $\mathbf{L}$ the approximation of the Laplace-Beltrami operator. The result of grid regularization obtained after 20 iterations of (3) is shown in Fig. (3). The value of γ is 1.24 for the grid of level four which is slightly better than that for the case of spring dynamics even with the nonlinear relation for k. The further comparison of both methods is currently investigated in order to establish the best grid regularization technique.

The quality of a regularized grid can be verified by investigation of the approximation error of ∇, div and $\nabla\times$ operators. We use the test functions $\alpha(\lambda, \theta) = \sin(\lambda)$, $\beta(\lambda, \theta) = \cos(m\lambda)\cos^4(n\theta)$, $\mathbf{u} = \alpha\nabla\beta$ with $m = 3$ and $n = 3$ and calculate $\nabla \mathbf{u}$, $\hat{\mathbf{k}}(\nabla \times \mathbf{u})$ and $\nabla\beta$ using the approximation described in Pudykiewicz (2006). The convergence of l_2 and l_∞ error norms for these operators on grids regularized by iterating relation (3) is shown in Figs. 4–6 (l_2 is indicated by squares, l_∞ by triangles, the results for standard icosahedral grids are denoted by dashed lines; the red line indicates the second order convergence).

REFERENCES

Pudykiewicz J., 2006, *J. Comp. Phys.*, **213**, 358-390.

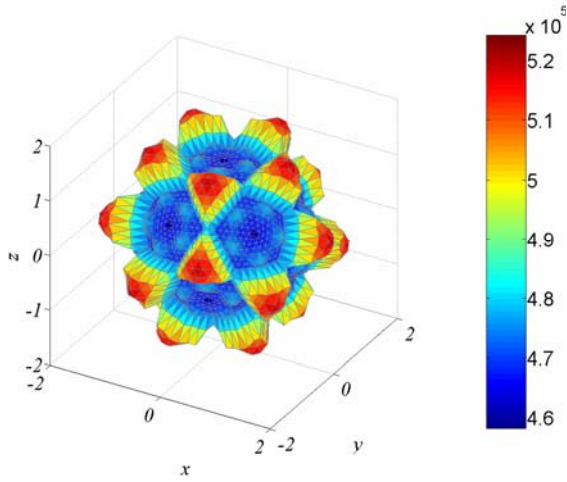Tomita H., M. Tsugawa, M. Satoh, K. Goto, 2001, *J. Comp. Phys.*, **174**, 579-613.

Fig.1 Surface: $(1 + (\delta - \delta_{min})/(\delta_{max} - \delta_{min}))$ for the grid of level 4; (δ is the mesh interval)
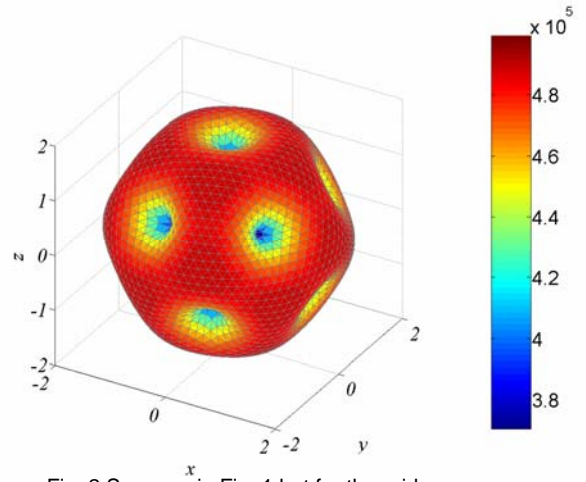

Fig. 2 Same as in Fig. 1 but for the grid regularized using the spring dynamics method
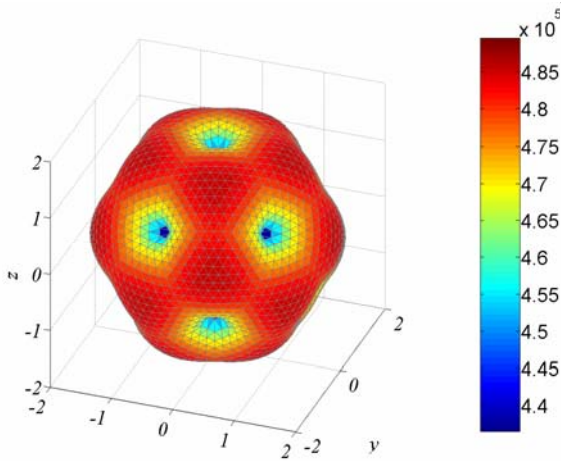

Fig. 3 Same as in Fig. 1 but for the grid regularized using the relation resulting from Gauss "Theorema Egregia"
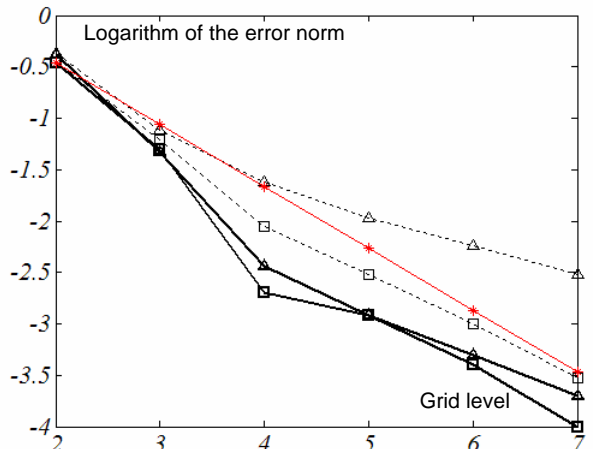

Fig. 4 The convergence of error norms for the gradient operator
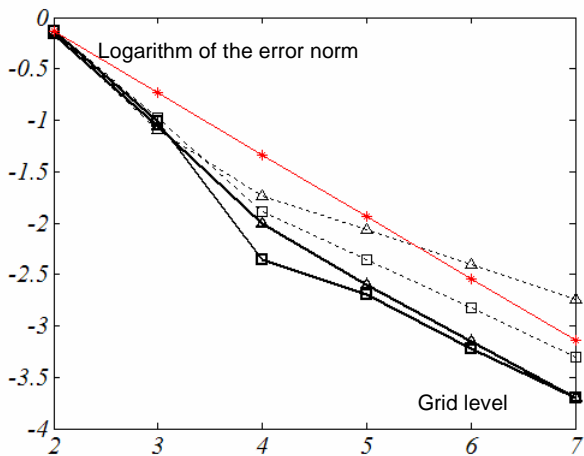

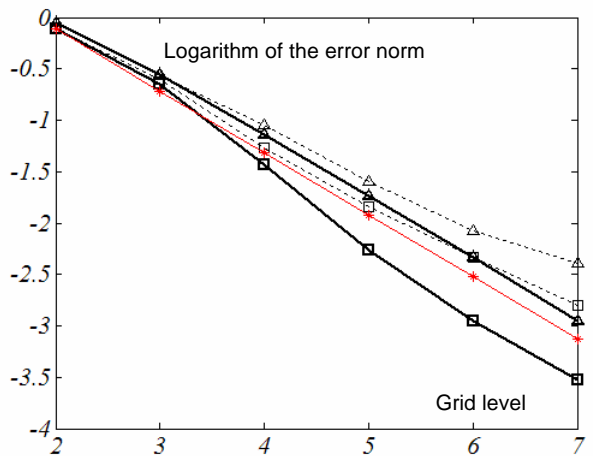Fig. 5 The convergence of error norms for the divergence operator

Fig. 6 The convergence of error norms for the rotation operator

Implementation of lateral boundary perturbations into mesoscale EPS

Kazuo Saito*, Masaru Kunii*, Hiromu Seko*,
Munehiko Yamaguchi ** and Kohei Aranami**
* Meteorological Research Institute, Tsukuba, Ibaraki 305-0052, Japan; ksaito@mri-jma.go.jp
** Numerical Prediction Division, Japan Meteorological Agency

In the previous report (Saito et al., 2007a), a BGM method for mesoscale ensemble prediction was presented where the JMA nonhydrostatic model (NHM) with a horizontal resolution of 10 km was employed. Targeting the 2004 Niigata heavy rain event, 12 hourly self breeding cycles were conducted from 12 UTC 09 July to 12 UTC 12 July 2004, using the moist total energy norm by Barkmeijer et al. (2001) to normalize the bred vectors. The variation of rainfall amount in the initial stage (FT=0-6), which was too large in the simple downscaling method of the JMA's operational global EPS (WEP), was reduced while in the later half of the forecast period (FT=12-18) the variety of precipitation amount reached 2 times in averaged values and 3 times in peak values. On the other hand, prior to the 2007 preliminary experiment in the WWRP Beijing Olympic 2008 Research and Development Project (B08RDP), we tested a similar self BGM method but no distinct gain was found in the tested BGM method compared with WEP in the growth of the ensemble spread for surface conditions. Two 12 hourly self breeding cycles were employed in the tested B08RDP BGM method using the perturbations of WEP in the day before as the initial seed.

In the MRI/JMA EPS, lateral boundary conditions were given by the forecast of the JMA's regional NWP (RSM) and perturbations in the lateral boundary were neglected. Without the lateral boundary perturbations, regional bred vectors may tend to become similar if some appropriate orthogonalization is not applied. In the ensemble Kalman filter (EnKF), the forecast error covariance may be underestimated near the lateral boundary, which yields underestimation of Kalman gain in the assimilation of observed data. In B08RDP, most participants use forecasts of global EPSs for lateral boundary conditions, however use of low resolution global EPS forecasts enlarges the resolution gap at lateral boundaries. Besides, the forecast values from the JMA one week global EPS are sent to MRI as the thinned pressure plane files; 1.25 degrees and 11 planes for the RSMC Tokyo responsible area (RSMC125 file).

In order to overcome above problems, we developed an incremental boundary perturbation method where the perturbations by the RSMC125 file are added to the model plane forecast values by the high resolution deterministic global forecast (TL959L60) of JMA. The RSMC125 file consists of 11 level pressure planes and surface plane data which cover RSMC Tokyo responsible area (90 E - 180E and 0N -71.25N) with 6 hourly forecast output. The initial and forecast ensemble perturbations on NHM model planes are computed by subtracting the interpolated values of the control run from the interpolated values of the ensemble members. Since the highest level of the RSMC125 file is 100 hPa, perturbation increments above 100 hPa level in the NHM model plain are computed by extrapolation and set to zero at the model top of NHM.

Result of a downscale ensemble experiment for 12 UTC 14 January 2008 is shown, where initial condition is the JMA mesoscale analysis (MA) and the lateral boundary condition of control run is the forecast of high resolution GSM (TL959L60). The initial and lateral perturbations are given by the RSMC125 file. Other specifications are almost same as the B08RDP experiment (15 km L40, 11 members) except the model domain (Japan area, 3000 km x 2700 km).

Figure 1 shows ensemble spread (root mean square errors from the ensemble mean) of horizontal wind (U) at z*=1.46 km level when the perturbations are not added to the lateral boundary conditions. The spread is relatively large along the convergence zone over the western central part of the Japan Sea, which indicates that the forecast results tend to diverse at positions of disturbances, however, the spread decreases in the lateral boundary relaxation areas (24 grids in each side) after the start-up (Fig. 1a), and the influence of lateral boundaries propagates inside of the model domain with the time. At FT=24 (Fig. 1b), spreads over disturbance free areas become very small, such as less than 0.5 m/. Figure 2 shows the ensemble spread when incremental perturbations are added to the lateral boundary conditions. In this case, even at FT=24, areas of large ensemble spread are seen throughout the entire model domain including the

East China Sea (Fig. 2b). Spread over the western central part of the Japan sea is larger and extends to more wide areas. Figure 3 shows time sequence of area averaged ensemble spreads over the central part of the model domain. Differences of spreads with and without lateral perturbations are distinct after FT=12 and become more than twice at FT=36.
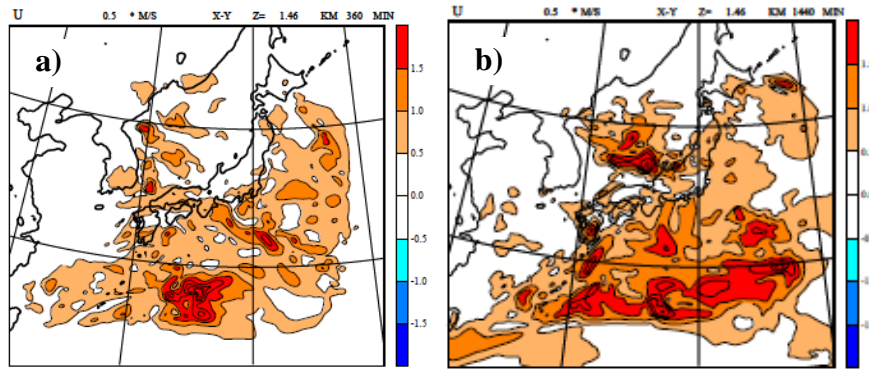
Fig. 1. Spread of horizontal wind with the 11 member mesoscale ensemble prediction. Perturbations are not added to the lateral boundary conditions. **a)** FT=6. **b)** FT=24.
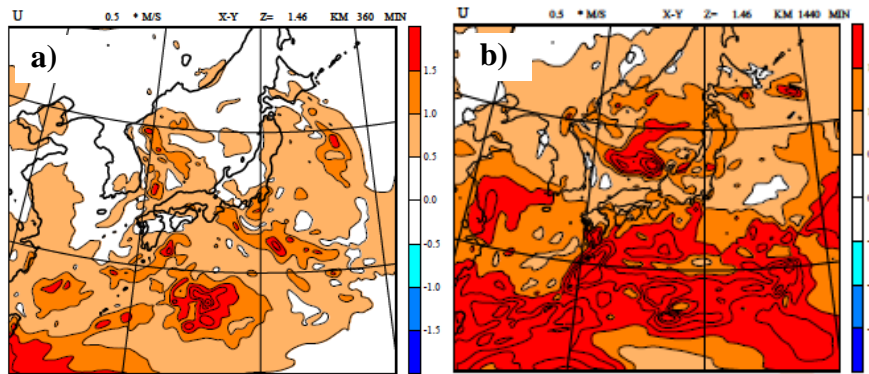
Fig. 2. Same as in Fig. 1, but incremental perturbations are added to the lateral boundary conditions.
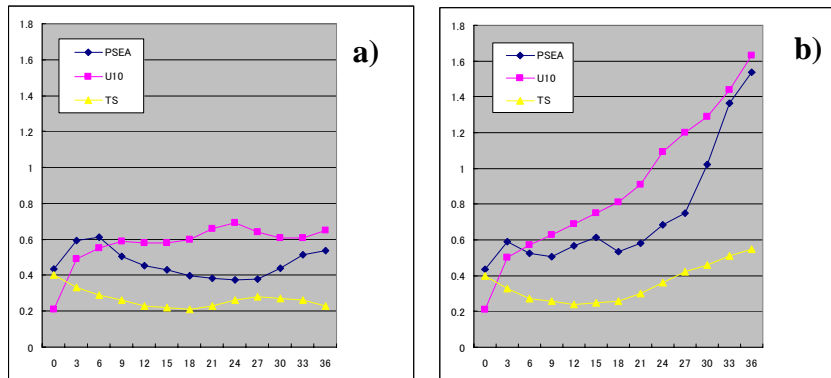
Fig. 3. Time sequence of area averaged ensemble spreads over the central part of the model domain (a rectangle of 1000 km square). **a)** Perturbations are not added to the lateral boundary conditions. **b)** incremental perturbations are added to the lateral boundary conditions. (Psea; Mean sea level pressure, U10; Horizontal wind at 10m, TS=Surface temperature). In these comparative experiments, no perturbations are used in soil temperatures.

References

Saito, K., 2007a: Development of a BGM method with the JMA nonhydrostatic mesoscale model. *CAS/JSC WGNE Research Activities in Atmospheric and Oceanic Modelling.* **37**, 5.27-5.28.

Saito, K., H. Seko, M. Kunii, T. Hara, M. Kyouda and M. Yamaguchi, 2007b: Preliminary Mesoscale Ensemble Prediction experiment for WWRP Beijing 2008 RDP. *CAS/JSC WGNE Research Activities in Atmospheric and Oceanic Modelling.* **37**, 5.25-5.26.

Finite-element scheme for the vertical discretization of the global semi-lagrangian SL-AV model

A. Shlyaeva[1], M. Tolstykh[1,2]
e-mail: shlyaeva@gmail.com, tolstykh@inm.ras.ru

[1] Hydrometeorological Research Center of Russia, Moscow, Russia
[2] Institute of Numerical Mathematics, Russian Academy of Sciences, Moscow, Russia

The global semi-lagrangian NWP model SL-AV [1] was developed in Hydrometeorological Research Center of Russia and Institute of Numerical Mathematics, Russian Academy of Sciences. The horizontal resolution of the model is 0.9° in longitude and 0.72° in latitude; currently there are 28 vertical levels. Model variables are vertical component of the absolute vorticity, horizontal divergence, temperature, surface pressure and specific humidity. Subgrid scale parametrizations developed in Meteo-France for ARPEGE/IFS [2] model are used.

SL-AV model validation carried out in Hydrometcentre of Russia revealed significant negative geopotential bias in the stratosphere. It is known [3] that possible reason of this bias is poor accuracy of integration of the hydrostatic equation. Untch and Hortal [3] implemented finite-element integration scheme instead of finite-difference midpoint rule and achieved significant reduction of the bias in the stratosphere.

SL-AV model previously integrated hydrostatics equation via trapezoidal rule. The analysis showed that the trapezoidal rule is more accurate than midpoint rule, however, both methods are less accurate than finite-element method with piecewise linear basis functions. Table 1 contains RMS error of the integration for $\sin 6\pi x$ function via the above methods on the 50, 100 and 150 uniform spaced levels.

Table 1

Number of points	Trapezoidal rule	Midpoint rule	Finite-element method (linear basis functions)
50	5.4575E-4	6.6815E-4	2.9030E-5
100	1.3614E-4	1.6671E-4	1.8708E-6
150	6.0480E-5	7.4069E-5	3.6577E-7

According to the table, the finite-element method is 4th order accurate while both finite-difference methods are 2nd order accurate. Furthermore, it is strictly proven that for uniform grids linear finite-element scheme is 4th order accurate [5].

Due to its high accuracy property, the finite element integration method was implemented in the SL-AV model. Hydrostatic equation and continuity equation are concerned. Two 30-day series of 120-hour forecasts for August 2005 and December 2005 using two versions of SL-AV model (with vertical integration via trapezoidal rule and via finite-element method) were calculated. The starting point for the forecasts was the analysis from [6]. The first guess is 6-hour SL-AV model forecast starting from the previous assimilation step.
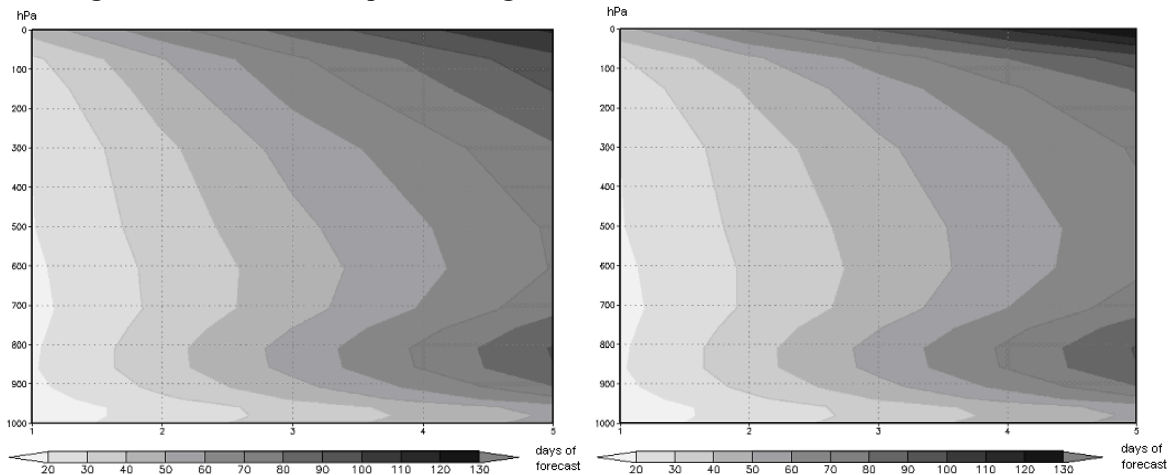
Southern hemisphere averaged geopotential bias is shown in Figure 1 (finite-difference method on the left and finite-element on the right) while Southern hemisphere averaged root-mean square errors are shown in Figure 2.

One can see that integration via finite-element method reduces bias and root-mean square error in the stratosphere and upper troposphere. The results obtained from the series of forecasts of December 2005 in the Northern hemisphere are similar to the above.

Over the summer hemisphere for both (August 2005 and December 2005) forecast series bias is reduced in the upper troposphere and in the stratosphere while in the upper stratosphere positive bias is observed.
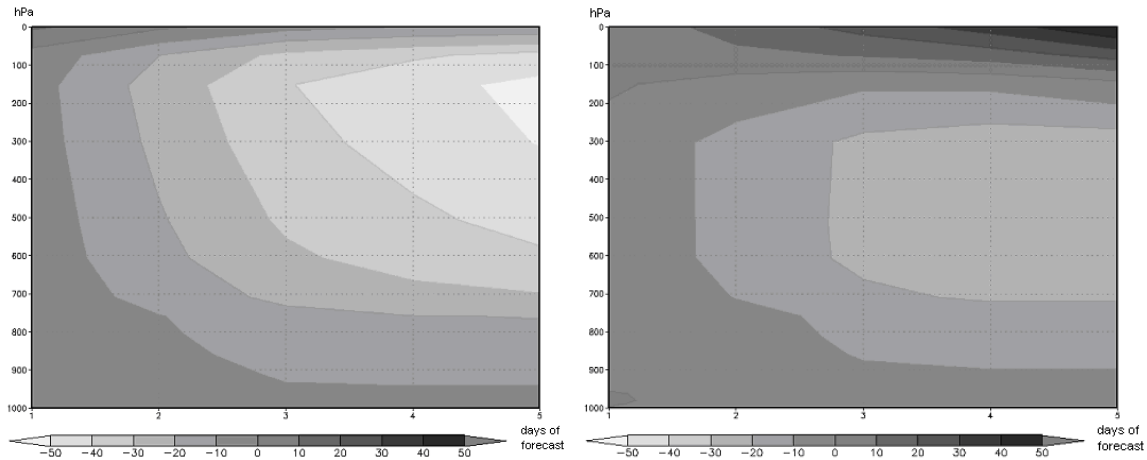
Figure 1 – Southern hemisphere averaged bias (left – finite-difference, right – finite-element)

Figure 2 – Southern hemisphere averaged RMS (left – finite-difference, right – finite-element)

References

1. Tolstykh M. Semi-Lagrangian high resolution model of the atmosphere for numerical weather prediction. – Russian Meteorology and Hydrology, 2001, N4 , pp. 1-9.

2. Geleyn, J.-F., Bazile, E., Bougeault, P. et al. Atmospheric parameterization schemes in Meteo-France's ARPEGE N.W.P. model. - In "Parameterization of subgrid-scale physical processes", ECMWF Seminar proceedings, 1994, pp. 385-402.

3. A.Untch, M.Hortal. A finite-element scheme for the vertical discretization of the semi-Lagrangian version of the ECMWF forecast model. Quart. J.Roy. Met. Soc., 2004, 130, pp. 1505-1530.

4. Tolstykh M.A. Vorticity-divergence semi-shallow-water model on the sphere based on compact finite-differences. - J. of Comput. Phys, 2002, v. 179, pp. 180-200.

5. Staniforth, A., Wood, N. Comments on 'A finite-element scheme for the vertical discretization in the semi-Lagrangian version of the ECMWF forecast model' by A. Untch and M. Hortal (April B, 2004, 130, 1505-1530). – Q.J.R. Meteorol.Soc., 2005, 131, pp.765-772.

6. M.D. Tsyryulnikov, M.A. Tolstykh, A.N. Bagrov, R.B. Zaripov. - Development of a global data assimilation system with variable resolution. - Russian Meteorology and Hydrology, 2003, N4, pp. 5-24.

Implementation of the reduced grid in the shallow-water prototype of the global finite-difference SL-AV model

Mikhail Tolstykh,
Institute of Numerical Mathematics Russian Academy of Sciences,
and Hydrometcentre of Russia, Moscow Russia
Email: tolstykh@inm.ras.ru

Today, many global spectral models apply the reduced grid (i.e. the grid where the number of points in longitude is gradually reduced while approaching the poles). The construction of the global finite-difference semi-Lagrangian SL-AV model [1] enables the implementation of the reduced grid: some part of calculations is carried out in space of Fourier coefficients in longitude. Also, the semi-Lagrangian advection is used (so there are no nonlinear advective terms). Necessary latitudinal derivatives (i.e. geopotential gradient) can be calculated in Fourier space. The algorithm for construction of reduced grids for a finite-difference semi-Lagrangian model was developed by R. Fadeev in [2]. It is based on the estimation of accuracy for semi-Lagrangian interpolation on the sphere and takes into account that the number of grid points at each latitudinal circle should be suitable for FFT.

Explicit terms of dynamics equations and semi-Lagrangian advection are calculated on the reduced grid. Calculation of nonlinear terms in the grid-point space requires some averaging, which is difficult to calculate on the reduced grid. Nonlinear terms are calculated on the full grid and then interpolated to the reduced one. Calculations in Fourier space are carried out as in the case of the full grid. At the end of these calculations, some variables are restored on the full grid, others – on the reduced one.

The reduced grid was implemented and tested in the framework of the shallow-water prototype for the SL-AV model [3] with the standard test set by Williamson et al [4]. First, the grid was constructed in a somewhat arbitrary way; the reduction of total number of grid points was 20 %. The resolution was 1.5 degrees in longitude and latitude everywhere except high latitudes. Tests 2, 3, 6 and 7 were carried out. It turned out that the results of the tests are sensitive to the choice of the grid, especially for test 7a with `real' data, where there is a significant cross-polar flow - see Fig.1, curves 'full' and 'red'. Then the reduced grid calculated following [2] was used, with the relative reduction of total number of grid points 9.3 %. The proper construction of the reduced grid provides the results hardly distinguishable from the ones obtained with the full grid (curve 'new red' in Fig.1). Some grids constructed using [2] are shown in Fig.2. Further tests will be carried out using grids having more reduction.

It is planned to implement the reduced grid in the full 3D version of the SL-AV model.

References

1. Tolstykh M.A., Semi-Lagrangian high-resolution atmospheric model for numerical weather prediction, *Russian Meteorology and Hydrology*, 2001, N 4, P. 1 – 9.
2. Fadeev R., Construction of a reduced latitude-longitude grid for a global numerical weather prediction problem, *Russian Meteorology and Hydrology,* 2006, N9, P. 5-20 (Extended abstract in Research activities in atmospheric and oceanic modeling, Ed. J. Côté, Rep. No. 35, 2005, WMO/TD - 1276. P 3.09-3.10).
3. Tolstykh M., Vorticity-divergence semi-Lagrangian shallow-water model on the sphere based on compact finite differences*, J. Comput. Phys.* V. 179, (2002), 180-200.

4. Williamson D.L., Drake J.B., Hack J.J., Jakob R., and Swarztrauber P.N., A standard test set for numerical approximations to the shallow water equations in spherical geometry, *J. Comput. Phys.*, V. 102 (1992), P. 211-224.
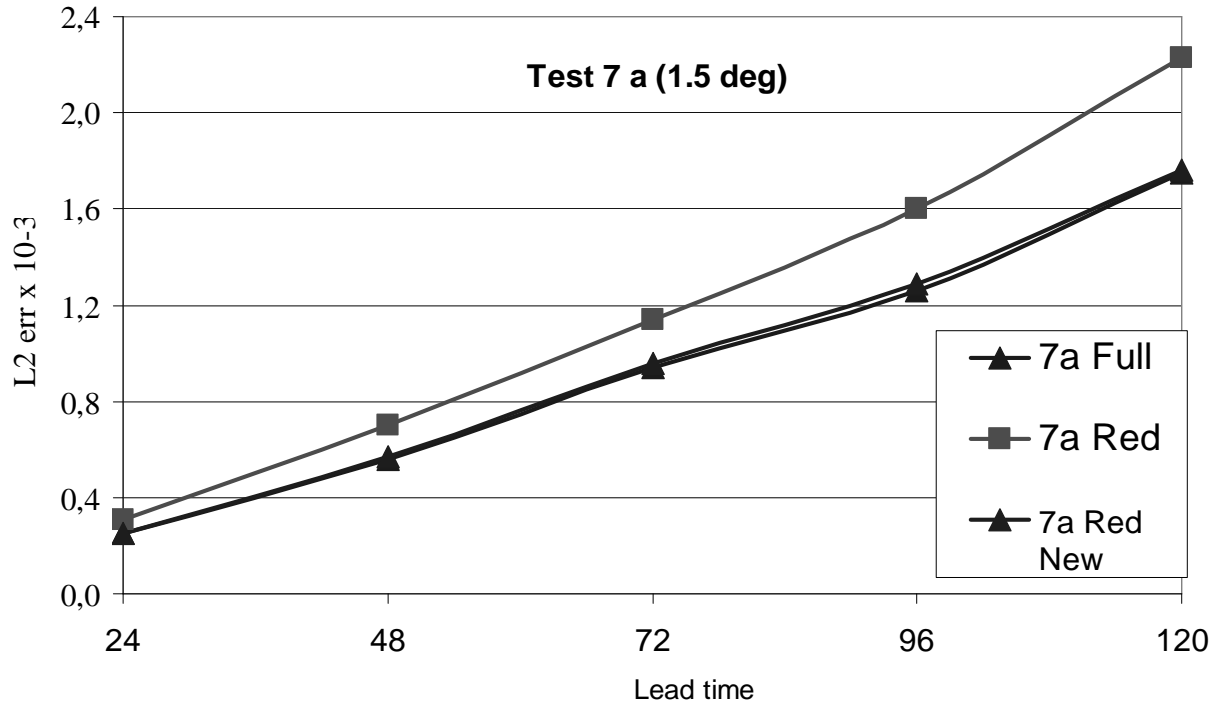
Figure 1. Global normalized height error vs time for Test 7a from [4] for full grid, the grid with the relative reduction of number of points by 20 %, and the reduced grid with the reduction by 9.3 % constructed with the algorithm [2].
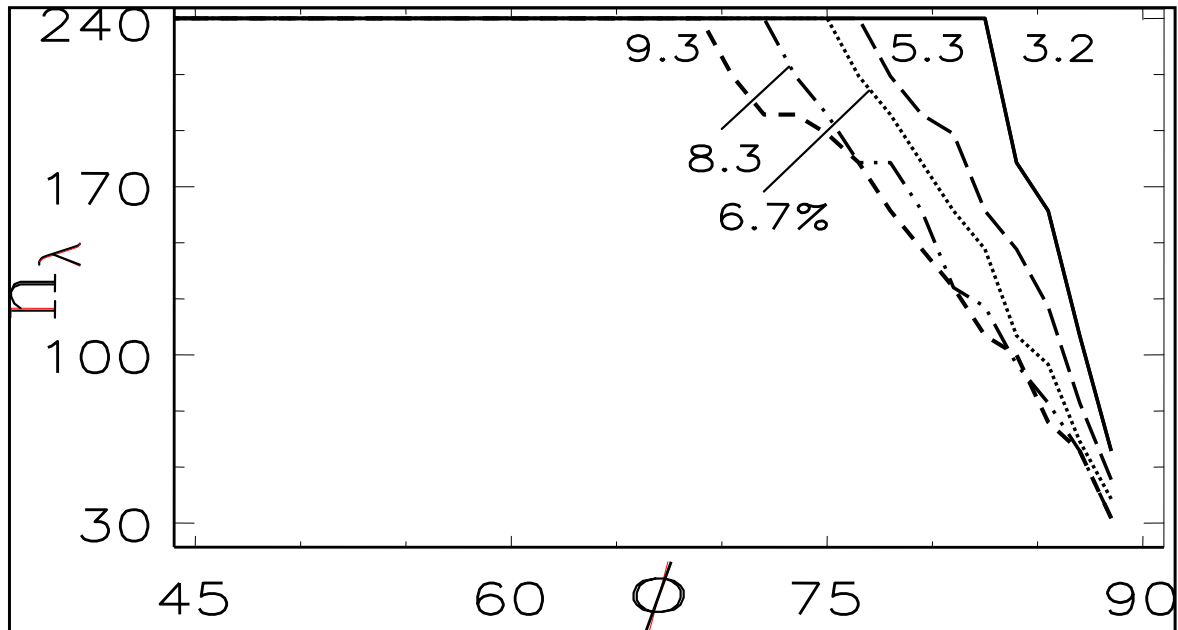

Figure 2. Number of grid points at given latitude circle as a function of latitude (in degrees) for different reductions (%) of total number of points. Grids are constructed with the algorithm [2].